The role of polaronic states in the enhancement of CO oxidation by single-atom Pt/CeO_2

Minttu M. Kauppinen[1,2 †], Nathan Daelman[3,†], Núria López[3], and Karoliina Honkala[1]

[1]*Department of Chemistry, Nanoscience Center, University of Jyväskylä, P.O. Box 35, FI-40014, Jyväskylä, Finland.*

[2]*Department of Physics and Competence centre for Catalysis, Chalmers University of Technology, SE-412 96 Göteborg, Sweden.*

[3]*Institute of Chemical Research of Catalonia (ICIQ), The Barcelona Institute of Science and Technology (BIST), Av. Països Catalans 16, 43007 Tarragona, Spain.*

[†]*These authors equally contributed to this work.*

June 2, 2022

Abstract

Single Atom Catalysts (SACs) have shown that the miniaturization of the active site implies new phenomena like dynamic charge transfer between isolated metal atoms and the oxide. To obtain direct proof of this phenomenon is challenging, as many experimental techniques provide averaged properties or have limitations with poorly conductive materials, leaving kinetic measurements from catalytic testing as the only reliable reference. Here we present an integrated Density Functional Theory-Microkinetic model including ground and high-energy metastable states to address the reactivity of Pt_1/CeO_2 for CO oxidation. Our model agrees with experimentally available kinetic data showing that CO oxidation activity of Pt_1/CeO_2 is tunable via the electronic properties of the support. Particularly, samples with higher n-doping via oxygen depletion should be better in CO oxidation, as they help maintain the active state Pt^0 of the catalyst. This provides a general route to improve low-temperature oxidations at metal/oxides interfaces via charge transfer control.

Introduction

Single Atom Catalysts (SACs) have emerged as a new class of materials that bridges heterogeneous and homogeneous catalysis, benefiting from the properties of both[1,2]. The field was inaugurated by the report of the enhanced CO oxidation activity of individually deposited Pt atoms on reducible iron oxide, FeO_x[3]. In the years following, the number of SAC applications has tremendously increased[1,4–6]. The miniaturization of the active sites comes with a strong electronic coupling between the metal atom and the host. Thus, the electronic states of the metal[7] are better represented as an electronic ensemble, formed by ground and metastable high-energy states, with Pt in different oxidation states.

The Pt/CeO_2 system, in particular, has been extensively studied as a novel candidate catalyst for low-temperature oxidation in the three-way automotive exhaust post-processing[8–15], which covers the full combustion of CO and hydrocarbon and elimination of NO_x. Initially, these materials were thought to be constituted by rather small active nanoparticles (diameter$< 1.4\,\mathrm{nm}$)[10,11,16]. But reports of outstanding reactivity while preserving the dispersion[13,14,17,18], suggesting that the SACs themselves are the real active state. Kinetic experiments show that light-off CO oxidation over as-prepared Pt_1/CeO_2 reaches full conversion at $250^\circ\,C$[19]. An activation step with reductive CO pulses boosts its reactivity further[11,19] lowering the full conversion temperature to $175^\circ\,C$[20] and the apparent activation barrier between 0.3 and $0.4\,\mathrm{eV}$[11]. The extent of this activity enhancement varies with reductant gas (hydrogen[21], steam[14,22]) and temperature, but remains significant throughout. The as-synthesized dispersed SA Pt are known to be ionic (2+) with a four-fold oxygen coordination created through oxidative treatments either at stepped or nanostructured CeO_2 surfaces, as confirmed by XPS and IR[8,23]. However, tracking the state of SAs in operando faces the limits of atomic-resolution microscopy and spectroscopy techniques[24,25]. This leaves experimental kinetics, i.e. the conversion rates and activation energies, as the most reliable benchmark for comparing simulations.

To directly map the CO oxidation kinetic behaviour onto experiments we employ microki-

netic modelling (MKM)[26,27] based on the computed DFT reaction network and coupled to the external control variables, i.e. temperature and pressure, to obtain the time-evolution of the surface intermediates[28,29]. This approach is valid at low loadings, where the SAC can be thought of as isolated sites, thus equivalent to Kinetic Monte Carlo[30]. MKM is also a powerful analytics tool for retrieving the relevant catalytic domains[31], rate-determining steps, and surface coverages[29]. Furthermore, it enables descriptor-aided design[32,33], allows extensions towards high-pressure regimes[34] and can identify novel on-surface pathways[35]. Still, microkinetics are applied to the ground-state energy profile with singular, unique well-defined intermediates along the reaction coordinate[36]. While an extension to geometric ensembles has recently been considered for clusters[37], electronic ensembles have not yet been included.

In this work, we present a microkinetic model for CO oxidation by SA Pt/CeO_2, based on DFT data. In light of the dynamic change of the oxidation state of the Pt centre, we employ the electronic manifold in the MKM simulations. We show that only by including the electronic ensemble do we retrieve good agreement with experimental kinetics, allowing for new design concepts to emerge.

Computational Details

DFT Calculations

All energies and frequencies were computed using the Perdew-Buke-Ernzerhof (PBE) functional[38,39] as implemented in the Vienna Ab initio Simulation Package (`VASP`; version 5.4.4)[40–43]. Hence, the valence-electrons are modelled using a plane-wave basis set with a cutoff energy of 500 eV, while projector-augmented waves (PAW) describe the core-electrons[44]. The Brillouin zone was sampled using a gamma-centered, (3×3) k-mesh. Since regular GGA fails to capture the Density of States (DOS) in reduced rare-earth oxides[45], we employed a Hubbard correction with an effective on-site Coulomb interaction ($U_{\text{eff}} = 4.5\,\text{eV}$) to the Ce 4f-orbitals[7,46]. While d-band materials similarly suffer from erroneous self-energy, no

issues have been raised regarding the efficacy of GGA for diplatinum oxide (PtO_2, α and β phase)[47,48]. Moreover, the introduction of Hubbard correction can lead in and of itself to biases in the thermodynamics and kinetics of charge transfer processes[49]. Considering the cost-benefit analysis, we thus prefer to keep the usage of Hubbard corrections to a minimum.

CeO_2 has a fluorite structure with an experimental lattice parameter of 5.410 Å. All slab models are (3×3) supercells of nine atom layers thick cleaved along the (100) direction. Of these nine layers, the lower four were kept fixed to simulate the bulk. A vacuum height of 15 Å was chosen to allow enough space for adsorbates to adsorb. This results in unit cell dimensions of $11.649\,\text{Å} \times 11.649\,\text{Å} \times 25.983\,\text{Å}$. To simulate the spontaneous reconstruction of the surface after cleavage, half of the top surface oxygen atoms are moved to the bottom layer. The remaining surface atoms are aligned according to most stable termination, with parallel rows of oxygen atoms alternating with trenches of vacancy sites. This provides the single-atom metal with two ligands. The dipole moment is accounted for.

Transition states between different intermediates were obtained using climbing image NEBs[50] and verified by harmonic frequency analysis. Various intermediates were found to possess higher energy metastable states, where some cerium ions are reduced by electrons originating from Pt. The polaron hopping barrier, as modelled in Marcus Theory[51–53], exhibits two types of barriers, namely diabatic and adiabatic. In this work, we approximated the diabatic barrier similar to Ref. 54, i.e. by comparing the difference in energy between the states with a delocalized and localized electron. Note that in order to prevent volume-specific artefacts[55], unlike the reference, we did not charge our slab systems. Electron delocalization was instead enforced using the `NUPDOWN` keyword in `VASP`. Attempts to locally sample the PES as a parabola, as done in Ref. 53, were unsuccessful due to spurious electron localization along the propagation/reaction path. As such, we retrieve a polaron barrier of 0.37 ev for the jump from the neutral state to the most stable lattice site. This barrier lies within the same range of polaron hopping barriers observed on the (111) surface ($0.23 - 0.50\,\text{eV}$)[56], and is thus used as an estimate for polaron hops between other intermediates as well. The

sensitivity of the microkinetic model with respect to the polaron hopping barriers was tested by increasing each hopping barrier one at a time by 0.2 ev and observing the response in the results. It was found that changing the barriers by 0.2 ev had no effect on TOFs, coverages, or cycle selectivities. This is consistent with the finding that the hopping steps do not have rate controlling character.

Microkinetic Model

The set of elementary reactions included in the mean-field microkinetic (MFMK) model is represented diagrammatically in Fig. 1. For a list of elementary reactions and their labels, please refer to Table S3. The rate constants were calculated via Harmonic transition state theory using ZPE and entropy corrected activation free energies obtained from DFT calculations detailed in the previous section. To ensure thermodynamic consistency, the backward rate constants were calculated by dividing the forward rate constant by the equilibrium constant for each given elementary step. Furthermore, the total energies obtained from DFT for the gas-phase molecules were corrected in order to achieve a more accurate value for the total reaction energy (please see section 3 of SI for numerical values and details). The entropies of the surface species were calculated in the harmonic limit as implemented in the HarmonicThermo class of the ASE Thermochemistry package, while the entropies for the gas-phase species were calculated in the ideal-gas limit using the IdealGasThermo class of the ASE Thermochemistry package.[57,58]

The Pt/CeO_2 active sites can be assumed to be very isolated from each other, as the Pt atom is reasonably firmly anchored to its ideal location on the CeO_2 support. The adsorbate-adsorbate interactions are included explicitly in the underlying DFT calculations. Thus, in our case the mean-field microkinetic model and a fully spatially resolved Kinetic Monte Carlo (KMC) model will yield equivalent results[30,59] removing the typical limitation, i.e. lack of lateral interaction effects, for MFMK models.

The system of differential equations was solved using our own Python-based script. The

integration was carried out numerically with the solve_ivp function implemented in the Scipy package[60] scipy.integrate. The simulations were carried out at steady reaction conditions (i.e. constant temperature and pressure) for two different gas-phase compositions mimicking lean and very lean conditions. Each simulation was carried out for a long enough time (10^5 seconds in general) to ensure that the steady-state was reached before the end of the simulation. To test the influence of the polaron hopping steps, additional simulations were performed with all polaron hopping barriers set to 3 eV higher than in the standard simulations. This ensures that the reaction cannot proceed through these elementary steps at the temperatures considered here. Arrhenius plots (Fig. 4) were generated for each composition in the temperature range from 100 to 160° C, a range where the logarithm of the turnover frequency (TOF) can be expected to vary linearly with inverse temperature based on previous experiments[20]. For additional detail, please refer to section 2 of the SI.

Results and Discussion

Overview DFT Mechanism

The reaction network for the $2\,CO + O_2 \longrightarrow 2\,CO_2$ is shown in Fig. 1 and the corresponding PBE+U energy profile in Fig. S1. The name convention of species used throughout the work is explained in Section S1.3 and listed in Table S1. The reaction consists of two partially overlapping cycles: the shorter Cycle I revolves around the two-fold oxygen-coordination of the catalyst decorated by carbon-rich ligands, while the more oxygen-rich Cycle II switches coordination between two-fold, linear (2-s-oxo-Pt, II.1) and four-fold, square-planar (4-s-oxo-Pt, II.8) geometries. Surface species, such as 2-s-oxo-Pt (II.1) or carbonyl-2-s-oxo-Pt (A.4), exchange electrons with the lattice and thus exhibit multiple SA metal oxidation states (mOS) corresponding to separate potential energy surfaces (PES) for the CO oxidation reaction. The change in mOS can happen either by polaron hopping (with energy barrier) or be chemically induced by adsorption of ligands (likely involving entropic barriers), see

Methods and Sections S1.1 and S1.2. The reaction network shows that with increasing ligands coverage on Pt, the PES tend to converge to a single electronic state corresponding higher metal charge.

Cycle I: CO-protective Mechanism

Both cycles share a CO oxidation step (the carboxyl-mediated pathway) and diverge at the integration of an external oxygen source into carbonyl-2-s-oxo-Pt (A.4). In Cycle I, this is achieved via molecular O_2 absorbing as a surface peroxo (O_2^{2-}), which gains two electrons by oxidizing the vicinal metal centre to Pt^{2+} throughout most of the cycle. The surface peroxo, when anchored into the lattice, introduces local strain (Fig. S2). It is, however, also uniquely positioned to act as a peroxo ligand for the SA metal. Its predisposition hereto is supported by the drastic increases in dispersion levels and sintering resistivity at significant peroxo coverages[61]. Due to its mOS and four ligands, the I.1 complex is attempting to enforce a square-planar geometry, and we observe a considerably wide $\widehat{\text{C-Pt-O}}$ angle (117°) that hampers the reaction of the carbonyl with the peroxo. This in turn leaves the metal centre open to a nucleophilic attack of the second gas-phase CO, which forms a more advantageous 53° angle with the peroxo species in I.2. Since peroxo is already activated, the O−O bond breaks upon the formation of a PtOC−OO activated complex ($TS_{I.3}$) and leads to immediate CO_2 desorption with an activation barrier of ($E_a = 0.21\,eV$). The strain induced by the peroxo has disappeared in I.4 (Fig. S2), and as the lattice returns to equilibrium, it pushes the remaining oxygen ion (O^{2-}) towards Pt (A.1).

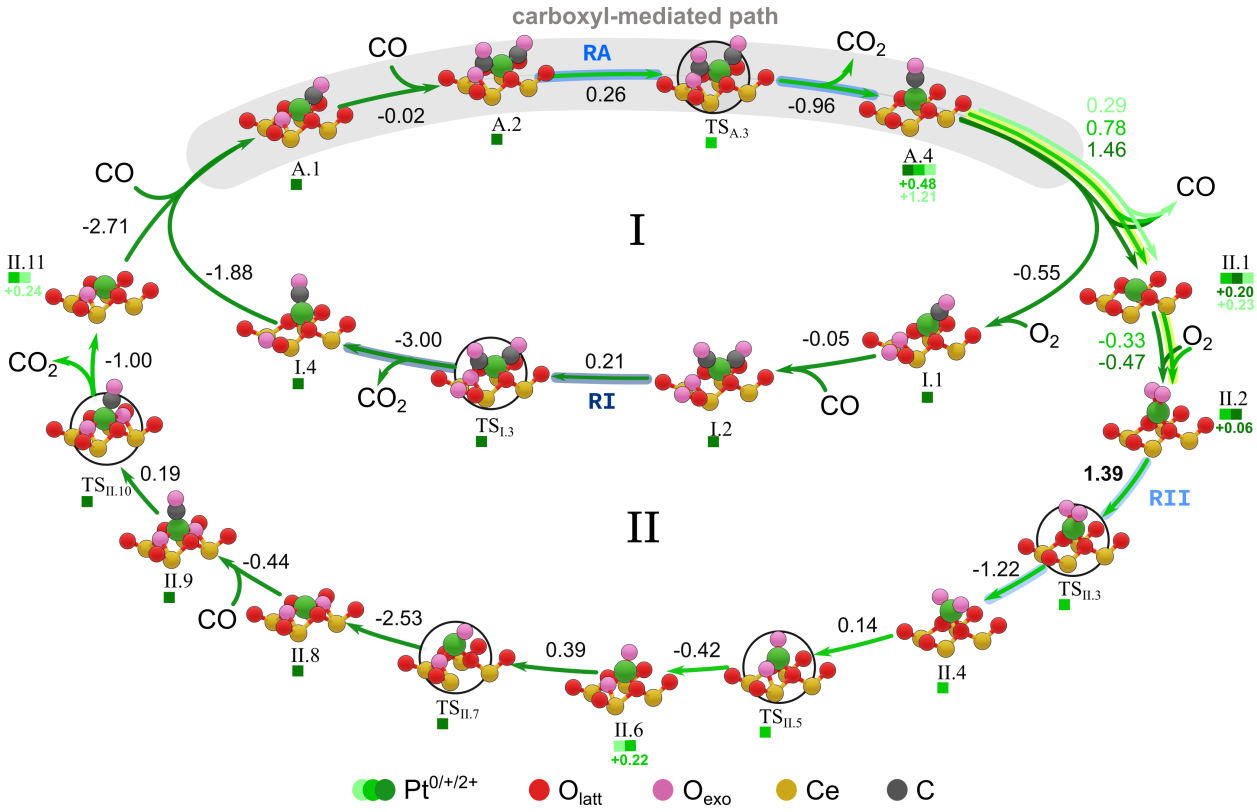

Fig. 1: Reaction network for CO oxidation over single-atom Pt_1/CeO_2 with the relative energy at each step. Depending on the atmospheric composition, the reaction progresses along one of two cycles (I: carbon-rich/II: oxygen-rich) that converge at the carboxyl-mediated path (grey shade). The intermediates and transition states (circled) local geometry -the metal complex and top surface layer- with their index and the Pt oxidation states as a footer (atomic colour code at the bottom). Oxidation states are ordered from left to right according to increasing electron transfer energy, referenced with respect to the ground state. Reactions with multiple PES follow the same conventions, and those with inhibited polaron hopping are highlighted in yellow. The rate-determining steps for each cycle, as determined by microkinetics, are highlighted in shades of blue, see text.

Carboxyl-mediated Pathway

The newly formed structure A.1 is analogous to I.1, but with an oxygen ion instead of peroxo, and the CO capture and conversion proceed similarly along the *carboxyl-mediated path*. To compensate for the wide angle (161°) in A.1, another carbonyl group is added, leading immediately to the formation of carboxyl-2-s-oxo-Pt intermediate (A.2), which is a clear structural precursor to CO_2. Thus, the activation barrier of 0.33 eV corresponds to Pt−C bond breaking ($TS_{A.3}$), which completes the full Cycle I. Note that in addition to

the two-fold coordination with the support, Pt always has a carbonyl ligand present, which functions as a protective group against direct oxidation during Cycle I.

Cycle II: Direct Oxidation

Cycle II starts with the removal of the protective carbonyl-group to obtain 2-s-oxo-Pt (II.1). The dynamic oxidation state, where several low-lying oxidation states change as a function of time, as verified by Born-Oppenheimer Molecular Dynamics[7], is most pronounced here due to quasi-degeneracy (energy span of 0.30 eV). Molecular O_2 now has space to chemisorb onto the unprotected metal centre and oxidize it to bidentate η_2-dioxo-2-s-oxo-$Pt^{+/2+}$ (II.2). The newly added ligands only bind with the metal but not the surface, thus significantly weakening the bond between the metal and its support weakens up to the point where Pt is lifted out of the surface plane by $0.92 - 1.01$ Å. In the next step, the O−O bond breaks ($TS_{II.3}$) with an activation barrier of $E_a = 1.39$ eV, the highest barrier in both cycles. The bond breaking forces the system into a single oxidation state, bis(oxo)-2-s-oxo-Pt^+ (II.4). For more information on both intermediates, see Section S1.4. The under-coordinated oxygen ligands in II.4 integrate one-by-one into the (100) trench orthogonal to $PtO_{2,upper}$ (Fig. S3). The following steps proceed via oxo-3-s-oxo-$Pt^{0/+}$ (II.6) with $E_a = 0.14$ eV to 4-s-oxo-Pt^{2+} (II.8), with $E_a = 0.40$ eV and an overall exothermicity of 2.40 eV.

To reactivate the square-planar resting state II.8, CO first adsorbs onto the metal centre, forming carbonyl-4-s-oxo-Pt^{2+} (II.9). Due to its orthogonal orientation to the square-planar ring, the carbonyl-ligand has a vantage point to attack one of the oxygen ligands ($TS_{II.10}$) and the resulting E_a is only 0.19 eV. CO_2 desorption breaks up the coordination shell and restores the oxidation state dynamics, producing a carbonyl-3-s-oxo-$Pt^{0,+}$ intermediate (II.11). At this point, Cycles I and II converge as the catalyst proceeds to the next the round of CO conversion.

DFT Takeaways

This concludes the analysis of Cycle I and Cycle II, which mainly differ in how they bind gas-phase oxygen, either near or at the metal site, leading to peroxo/superoxo which in turn affects the O−O bond activation. Subsequent CO oxidation steps proceed similarly in both cycles, and the DFT results suggest that Cycle II will contribute less to the conversion rates than Cycle I, due to the high O−O bond breaking barrier ($TS_{II.3}$). Thus based on DFT data we propose that the two-fold/four-fold coordinations correspond to the experimentally observed active/resting state of the catalyst [8,23].

Microkinetic analysis

The next step is to connect the reaction network to the experimental kinetic studies. Experiments have been conducted at a wide range of temperatures, pressure, and flow rates, due to the detailed analysis we will concentrate in the results in ref. [20]. To mimic the experimental conditions, we chose to simulate the reaction at atmospheric pressure with CO to O_2 ratios of 1 : 1 and 1 : 9, with 1e-5 bar CO_2. Simulations were carried out at temperatures ranging from 25 to 225° C at 10° C intervals. Note that the fractional coverage of a species is the fraction of SA occupied across the population of all SA sites.

Rate control

We performed a set of kinetic analyses for each gas-phase composition to assess the behaviour of the system. In order to determine which reaction steps are rate controlling, the degree of rate control, X_{rc}, was calculated for each elementary step in the reaction network. Three reactions (RI, RII, and RA, presented in Fig. 2) were found to have significant X_{rc} values (see Fig. 3), and thus control the overall CO_2 production rate throughout the whole temperature range considered. As the reactions RI and RII correspond to Cycle I and II, respectively, and RA is common to both cycle, the TOFs and X_{rc} values of RI and RII can be used to

determine which cycle dominates at any given reaction condition.

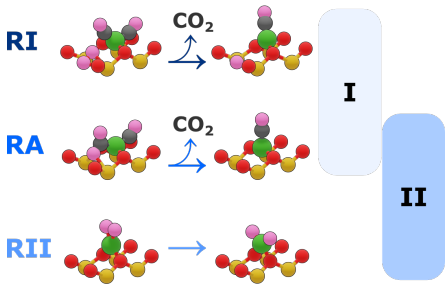

Fig. 2: Key steps RA, RI, and RII with significant rate control in the total reaction mechanism. The steps are also labeled in the cycle representation in Fig. 1.

At low temperature for both gas compositions, reaction RI is the most rate controlling, with an X_{rc} value of circa 0.65, while RA has an X_{rc} value of 0.35. This indicates that Cycle I is dominating at low temperatures, which is confirmed by a selectivity S_I value of one. As the temperature increases, the rate controlling character of RII increases further and goes through a maximum (c.a. 155° C for the 1 : 1 composition and c.a. 105° C for 1 : 9 see Fig. 3) before falling off at elevated temperatures. The X_{rc} value of RII starts to increase when the X_{rc} of RI has reached its maximum. The X_{rc} of RA initially decreases with increasing temperature, but starts to rapidly increase again at around 195° C for composition 1 : 1, whereas for the 1 : 9 composition the increase in X_{rc} starts already at 125° C. As Fig. 3 demonstrates, the fractional coverages of species I.1 and A.1, correlate extremely closely with the rate controlling character of RI and RA, respectively, because they are the reactant species of the steps immediately preceding them. For the composition 1 : 9, a slight offset is seen for the correlation between I.1 coverage and RI, whereas for composition 1 : 1 the correlation stays better. The correlation between X_{rc} and coverage remains throughout the whole temperature range for RA and A.1, and does not depend on gas ratio.

Cycle selectivity

The selectivity S_I towards Cycle I or S_{II} towards Cycle II are defined as $S_X = r_X/(r_I + r_{II})$ where 'X' stands for either I or II, and r_I/r_{II} is the rate of RI/RII. The resulting plot of

selectivities is presented in Fig. 3. The selectivity switch-over from Cycle I to Cycle II starts to occur concurrently with the fall/rise of the rate control of RI/RII. When $S_I = S_{II} = 0.5$, the rate control is also equally shared between RI and RII. This occurs at a much lower temperature for the 1 : 9 gas ratio. The switch-over from Cycle I to Cycle II is complete after RII has reached maximum rate control. At high temperatures the rate determining step (RII or RA) depends on the gas-composition, but there is no effect on the cycle selectivity when the rate control switches from RII to RA. The switch-over from Cycle I to Cycle II with rising temperature can be explained in terms of the stability of the CO ligand. Cycle I requires the presence of at least one CO ligand at all times for the reaction to proceed, but as the temperature increases (or CO partial pressure is lowered), desorption from the site becomes more favourable. The removal of the CO ligand forces the reaction to proceed through Cycle II.

Reaction orders

A low temperature for both gas compositions the reaction order with respect to CO starts at a constant value of 1, but rapidly starts to fall off towards zero at elevated temperatures. The curve perfectly traces the falling selectivity towards Cycle I. For the 1 : 9 gas-composition, the CO reaction order reaches a minimum at 155° C, then rapidly rising again and following the curve of the RA X_{rc} value. The positive reaction order of CO is rationalized as the RI and RA reactions proceed through intermediates with two CO molecules bound to the SA, therefore higher CO partial pressures will drive the reaction forward.

The reaction order with respect to oxygen is zero at low temperature for both compositions, as Cycle I is not as sensitive to the oxygen pressure. For the lean composition the reaction order rises following the Cycle II selectivity curve. The correlation is due to the most abundant surface species being the ligand free II.1 species. For the 1 : 9 composition the reaction order rises with temperature only slightly from zero. This is due to the rate controlling step being RA, which is not sensitive to oxygen pressure.

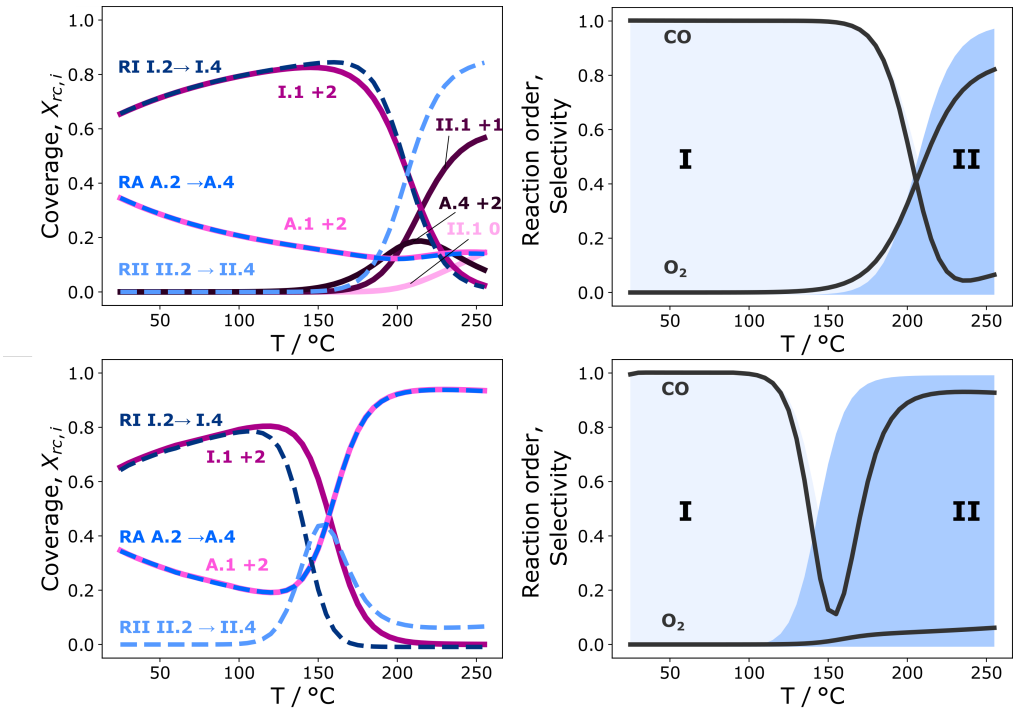

Fig. 3: Coverages of most abundant species (solid lines, see figure for assignment) and degrees of rate control (dashed lines marked RI, RII, and RA) as a function of temperature at 1 atm total pressure for 1 : 1 (top-left) and 1 : 9 (bottom-left) CO-to-O_2 ratios. Note that curves for rate control of RA and coverage of A.1 mOS 2 are directly on top of each other. Steady-state reaction orders of CO and O_2, and selectivities towards Cycle I and Cycle II as a function of temperature at 1 atm total pressure for 1 : 1 (top-right) and 1 : 9 (bottom-right) CO-to-O_2 ratios.

Comparison to experiments

Finally, Fig. 4 compares the turnover frequencies (TOF) obtained from the microkinetic models to previous experimental data from literature as a function of temperature. When the polaron hops are switched on, the reaction can proceed through Cycle I, which requires the SAC geometry A.4 to go from +I to +II in order to adsorb oxygen. When polaron hops are switched off, the reaction is forced to go through Cycle II, leading to lower TOF at low temperature (see insert in Fig. 4). At higher temperatures for the 1 : 1 gas-phase composition, the overall TOF is slightly lower when the polaron hops are switched on, due to the competition between Cycle I and Cycle II.

It is clear that a more oxidizing environment negatively impacts the overall performance,

attaining less than a third of the 1 : 1 TOF value at 250° C, and switching the polaron hopping steps off does not lead to an appreciable change in the overall TOF for the 1 : 9 composition. This may be due to the switch-over from Cycle I to Cycle II taking place at much lower temperature as compared to the 1 : 1 case. Once Cycle II starts up, the competition between the cycles is crucial for overall TOF. There are two conditions which enable Cycle I to compete with Cycle II: 1) polarons are switched on 2) CO removal is sufficiently unfavoured. With low CO pressure, removal of the protecting CO ligand is facile, which means that Cycle II dominates regardless if polarons are switched on.

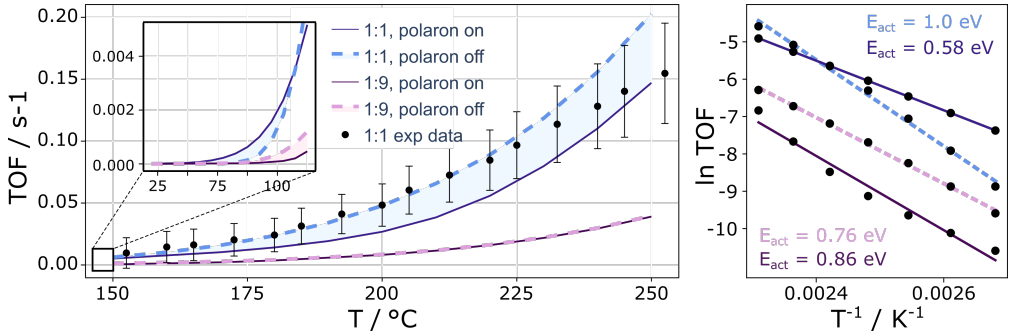

Fig. 4: Steady-state turnover frequency as a function of temperature at 1 atm total pressure for 1 : 1 (blue) and 1 : 9 (purple) CO-to-O_2 ratios. To measure the effect of the oxidation state dynamics, each setup has a model where polaron hopping is either turned *on* (full line) or *off* (dashed line). The hybrid region where polaron hopping is only partially active has been shaded. The inset shows the low temperature regime, where the boosting behaviour of each model interchanges. The experimental reference at 13 : 19 ratio (close to 1 : 1) is denoted by black dots with accompanying error bars. The Arrhenius plots for all four setups are presented on the right, using the same colour scheme as the TOF curves. Note that these data are computed from CO conversion rates in Ref. 20. For more information on how these data points were derived, see section *CO conversion rates to turnover frequency* in the SI.

The apparent activation energies (see Fig. 4) were determined to be 0.58 and 0.86 eV for the 1 : 1 and 1 : 9 compositions, respectively, which is in good agreement with previous observations of the experimental activation barriers ranging from 0.3 to 0.4 eV[11]. When polaron hopping steps are switched off, the corresponding apparent activation energies are 1.00 and 0.76 eV. The change in apparent activation energy observed for the 1 : 1 gas-phase composition when polaron hopping is not allowed, is a reflection of the switch over to the more energetically demanding Cycle II. For the 1 : 9 composition the change in the apparent

activation energy is minor, and the lower E_{act} obtained when polaron hops are allowed is probably due to the poorer linear fit as compared to the case when polaron hops are switched off. The presence of SAC oxidation state dynamics thus acts as a third reaction parameter, after the temperature and gas-phase composition. Considering the relationship between this parameter and the 4f-band filling of the support (see Table S3), a large enough concentration of Ce^{3+} ions should be able to suppress the dynamics and maintain SA Pt in a low oxidation state, increasing the yield substantially in the low-temperature regime. Experimentally, the bulk oxide reduction can be achieved by temperature treatment or dopants[62] . Our results show that experimental kinetics for reactivity of metals on semiconductor oxides need to account for the charge transfer dynamics and that the control of the defect states in the oxide can improve low-temperature oxidation paths.

Conclusions

A microkinetic model based on Density Functional Theory-computed energy profiles for CO oxidation on single Pt atoms on Ceria can be directly compared to experimental kinetics. However, to properly account for the charge transfer at the interface, the ground and low-lying potential energy surfaces need to be incorporated. Based on our model, we find that the catalytic process is characterized by two separate temperature and reactant sensitive reaction cycles (Cycle I and II). The dynamic charge transfer between the metal and the oxide enhances activity in the low temperature regime dominated by a Pt^0 active species (Cycle I). At high temperatures (over 225°C) the mechanism switches to being less sensitive to charge transfer dynamics (Cycle II). Thus, the low-temperature oxidation rate can be improved by controlling the prevalence of the metallic state through oxygen depletion in the bulk of the oxide. Our results highlight the need to consider the dynamical behaviour of the SAC mOS in order to produce computational models capable of qualitative agreement with experiments and point towards the control of charge transfer at metal/semiconductor

interfaces to improve oxidation processes.

Supporting Information Available

All DFT calculations have been made open-access at ioChem-BD[63]: https://iochem-bd.iciq.es/browse/review-collection/100/37388/edeeb937470b10f43b7528da. The MK data is available upon a reasonable request from the authors.

Acknowledgement

This work was funded by the Spanish Ministry of Economy and Competitiveness under the Mineco POP grant BES-2016-076361. The authors also thank the Barcelona Supercomputing Center (BSC-RES) for providing computational resources. Dr Marko Melander is acknowledged for careful reading of the manuscript.

References

(1) Wang, A.; Li, J.; Zhang, T. Heterogeneous single-atom catalysis. *Nat. Rev. Chem.* **2018**, *2*, 65–81.

(2) Mitchell, S.; Pérez-Ramírez, J. Single atom catalysis: a decade of stunning progress and the promise for a bright future. *Nat. Commun.* **2020**, *11*, 4302.

(3) Qiao, B.; Wang, A.; Yang, X.; Allard, L. F.; Jiang, Z.; Cui, Y.; Liu, J.; Li, J.; Zhang, T. Single-atom catalysis of CO oxidation using Pt_1/FeO_x. *Nat. Chem.* **2011**, *3*, 634–641.

(4) Liu, J. Catalysis by Supported Single Metal Atoms. *ACS Catal.* **2017**, *7*, 34–59.

(5) Kaiser, S. K.; Chen, Z.; Faust Akl, D.; Mitchell, S.; Pérez-Ramírez, J. Single-Atom Catalysts across the Periodic Table. *Chem. Rev.* **2020**, *120*, 11703–11809.

(6) Ginnakakis, G.; Mitchell, S.; Pérez-Ramírez, J. Single-atom heterogeneous catalysts for sustainable organic synthesis. *Trends in Chemistry* **2022**, to appear.

(7) Daelman, N.; Capdevila-Cortada, M.; López, N. Dynamic charge and oxidation state of Pt/CeO_2 single-atom catalysts. *Nat. Mat.* **2019**, *18*, 1215–1221.

(8) Jones, J.; Xiong, H.; DeLaRiva, A. T.; Peterson, E. J.; Pham, H.; Challa, S. R.; Qi, G.; Oh, S.; Wiebenga, M. H.; Hernández, X. I. P.; Wang, Y.; Datye, A. K. Thermally stable single-atom platinum-on-ceria catalysts via atom trapping. *Science* **2016**, *353*, 150–154.

(9) Wu, Q.; Ba, J.; Yan, X.; Bao, J.; Huang, Z.; Dou, S.; Dai, D.; Tang, T.; Luo, W.; Meng, D. Insight of Pt-support interaction in S-$Pt/Ce_{0.7}Zr_{0.3}O_2$ by in situ Raman spectroscopy. *Catal. Commun.* **2017**, *98*, 34–37.

(10) Gänzler, A. M.; Casapu, M.; Maurer, F.; Störmer, H.; Gerthsen, D.; Ferré, G.; Vernoux, P.; Bornmann, B.; Frahm, R.; Murzin, V.; Nachtegaal, M.; Votsmeier, M.; Grunwaldt, J.-D. Tuning the Pt/CeO_2 Interface by in Situ Variation of the Pt Particle Size. *ACS Catal.* **2018**, *8*, 4800–4811.

(11) Pereira-Hernández, X. I.; DeLaRiva, A.; Muravev, V.; Kunwar, D.; Xiong, H.; Sudduth, B.; Engelhard, M.; Kovarik, L.; Hensen, E. J. M.; Wang, Y.; Datye, A. K. Tuning Pt-CeO_2 interactions by high-temperature vapor-phase synthesis for improved reducibility of lattice oxygen. *Nat. Commun.* **2019**, *10*, 1358.

(12) Beniya, A.; Higashi, S. Towards dense single-atom catalysts for future automotive applications. *Nat. Catal.* **2019**, *2*, 590–602.

(13) Jeong, H.; Shin, D.; Kim, B.-S.; Bae, J.; Shin, S.; Choe, C.; Han, J. W.; Lee, H. Controlling the Oxidation State of Pt Single Atoms for Maximizing Catalytic Activity. *Angew. Chem. Int. Edit.* **2020**, *59*, 20691–20696.

(14) Jeong, H.; Kwon, O.; Kim, B.-S.; Bae, J.; Shin, S.; Kim, H.-E.; Kim, J.; Lee, H. Highly durable metal ensemble catalysts with full dispersion for automotive applications beyond single-atom catalysts. *Nat. Catal.* **2020**, *3*, 368–375.

(15) Boronin, A. I.; Slavinskaya, E. M.; Figueroba, A.; Stadnichenko, A. I.; Kardash, T. Y.; Stonkus, O. A.; Fedorova, E. A.; Muravev, V. V.; Svetlichnyi, V. A.; Bruix, A.; Neyman, K. M. CO oxidation activity of Pt/CeO_2 catalysts below 0°C: platinum loading effects. *Appl. Catal. B* **2021**, *286*, 119931.

(16) Maurer, F.; Jelic, J.; Wang, J.; Gänzler, A. M.; Dolcet, P.; Wöll, C.; Wang, Y.; Studt, F.; Casapu, M.; Grunwaldt, J.-d. Tracking the formation, fate and consequence for catalytic activity of Pt single sites on CeO_2. *Nat. Catal.* **2020**, *10*, 824–833.

(17) Lee, J.; Ryou, Y.; Kim, J.; Chan, X.; Kim, T. J.; Kim, D. H. Influence of the Defect Concentration of Ceria on the Pt Dispersion and the CO Oxidation Activity of Pt/CeO_2. *J. Phys.Chem. C* **2018**, *122*, 4972–4983.

(18) Yoo, M.; Yu, Y.-S.; Ha, H.; Lee, S.; Choi, J.-S.; Oh, S.; Kang, E.; Choi, H.; An, H.; Lee, K.-S.; Park, J. Y.; Celestre, R.; Marcus, M. A.; Nowrouzi, K.; Taube, D.; Shapiro, D. A.; Jung, W.; Kim, C.; Kim, H. Y. A tailored oxide interface creates dense Pt single-atom catalysts with high catalytic activity. *Energ. Environ. Sci* **2020**, *13*, 1231–1239.

(19) Gänzler, A. M.; Casapu, M.; Vernoux, P.; Loridant, S.; Cadete Santos Aires, F. J.; Epicier, T.; Betz, B.; Hoyer, R.; Grunwaldt, J.-D. Tuning the Structure of Platinum Particles on Ceria In Situ for Enhancing the Catalytic Performance of Exhaust Gas Catalysts. *Angew. Chem. Int. Ed.* **2017**, *56*, 13078–13082.

(20) Kunwar, D.; Zhou, S.; DeLaRiva, A.; Peterson, E. J.; Xiong, H.; Pereira-Hernández, X. I.; Purdy, S. C.; ter Veen, R.; Brongersma, H. H.; Miller, J. T.; Hashiguchi, H.; Kovarik, L.; Lin, S.; Guo, H.; Wang, Y.; Datye, A. K. Stabilizing High

Metal Loadings of Thermally Stable Platinum Single Atoms on an Industrial Catalyst Support. *ACS Catal.* **2019**, *9*, 3978–3990.

(21) Gatla, S.; Aubert, D.; Flaud, V.; Grosjean, R.; Lunkenbein, T.; Mathon, O.; Pascarelli, S.; Kaper, H. Facile synthesis of high-surface area platinum-doped ceria for low temperature CO oxidation. *Catal. Today* **2019**, *333*, 105–112.

(22) Nie, L.; Mei, D.; Xiong, H.; Peng, B.; Ren, Z.; Hernandez, X. I. P.; DeLaRiva, A.; Wang, M.; Engelhard, M. H.; Kovarik, L.; Datye, A. K.; Wang, Y. Activation of surface lattice oxygen in single-atom Pt/CeO_2 for low-temperature CO oxidation. *Science* **2017**, *358*, 1419–1423.

(23) Dvořák, F.; Farnesi Camellone, M.; Tovt, A.; Tran, N.-d.; Negreiros, F. R.; Vorokhta, M.; Skála, T.; Matolínová, I.; Mysliveček, J.; Matolín, V.; Fabris, S. Creating single-atom Pt-ceria catalysts by surface step decoration. *Nat. Commun.* **2016**, *7*, 10801.

(24) Li, X.; Yang, X.; Zhang, J.; Huang, Y.; Liu, B. In Situ/Operando Techniques for Characterization of Single-Atom Catalysts. *ACS Catal.* **2019**, *9*, 2521–2531.

(25) Liu, Q.; Zhang, Z. Platinum single-atom catalysts: a comparative review towards effective characterization. *Catal. Sci. Tech* **2019**, *9*, 4821–4834.

(26) Nørskov, J. K.; Studt, F.; Abild-Pedersen, F.; Bligaard, T. *Fundamental Concepts in Heterogeneous Catalysis*, 1st ed.; John Wiley & Sons, Inc.: Hoboken, New Jersey, 2014; p 196.

(27) Li, Q.; García-Muelas, R.; López, N. Microkinetics of alcohol reforming for H2 production from a FAIR density functional theory database. *Nat. Commun.* **2018**, *9*, 526.

(28) Bruix, A.; Margraf, J. T.; Andersen, M.; Reuter, K. First-principles-based multiscale modelling of heterogeneous catalysis. *Nat. Catal.* **2019**, *2*, 659–670.

(29) Saeys, M.; Reyniers, M. F.; Neurock, M.; Marin, G. B. Ab initio reaction path analysis of benzene hydrogenation to cyclohexane on Pt(111). *J. Phys. Chem. B* **2005**, *109*, 2064–2073.

(30) Alexopoulos, K.; Wang, Y.; Vlachos, D. G. First-Principles Kinetic and Spectroscopic Insights into Single-Atom Catalysis. *ACS Catal.* **2019**, *9*, 5002–5010.

(31) Kauppinen, M.; Melander, M.; Bazhenov, A.; Honkala, K. Unraveling the Role of the $Rh-ZrO_2$ Interface in the Water-Gas-Shift Reaction via a First-Principles Microkinetic Study. *ACS Catal.* **2018**, *8*, 11633–11647.

(32) Grabow, L. C.; Hvolbæk, B.; Falsig, H.; Nørskov, J. K. Search Directions for Direct H_2O_2 Synthesis Catalysts Starting from Au_{12} Nanoclusters. *Top. Catal.* **2012**, *55*, 336–344.

(33) Goulas, K. A.; Mironenko, A. V.; Jenness, G. R.; Mazal, T.; Vlachos, D. G. Fundamentals of C-O bond activation on metal oxide catalysts. *Nat. Catal.* **2019**, *2*, 269–276.

(34) Honkala, K.; Hellman, A.; Remediakis, I. N.; Logadottir, A.; Carlsson, A.; Dahl, S.; Christensen, C. H.; Nørskov, J. K. Ammonia Synthesis from First-Principles Calculations. *Science* **2005**, *307*, 555–558.

(35) Gokhale, A. A.; Dumesic, J. A.; Mavrikakis, M. On the mechanism of low-temperature water gas shift reaction on copper. *J. Am. Chem. Soc.* **2008**, *130*, 1402–1414.

(36) Wang, H.; Liu, J.-X.; Allard, L. F.; Lee, S.; Liu, J.; Li, H.; Wang, J.; Wang, J.; Oh, S. H.; Li, W.; Flytzani-Stephanopoulos, M.; Shen, M.; Goldsmith, B. R.; Yang, M. Surpassing the single-atom catalytic activity limit through paired Pt-O-Pt ensemble built from isolated Pt1 atoms. *Nat. Commun.* **2019**, *10*, 3808.

(37) Zhang, Z.; Zandkarimi, B.; Alexandrova, A. N. Ensembles of Metastable States Govern

Heterogeneous Catalysis on Dynamic Interfaces. *Acc. Chem. Res.* **2020**, *59*, 16527–16535.

(38) Perdew, J. P.; Burke, K.; Ernzerhof, M. Generalized Gradient Approximation Made Simple. *Phys. Rev. Lett.* **1996**, *77*, 3865–3868.

(39) Perdew, J. P.; Burke, K.; Ernzerhof, M. Erratum: Generalized Gradient Approximation Made Simple. *Phys. Rev. Lett.* **1997**, *78*, 1396.

(40) Kresse, G.; Hafner, J. Ab initio molecular dynamics for liquid metals. *Phys. Rev. B* **1993**, *47*, 558–561.

(41) Kresse, G.; Hafner, J. Ab initio molecular-dynamics simulation of the liquid-metalamorphous- semiconductor transition in germanium. *Phys. Rev. B* **1994**, *49*, 14251–14269.

(42) Kresse, G.; Furthmiiller, J. Efficiency of ab-initio total energy calculations for metals and semiconductors using a plane-wave basis set. *Comp. Mat. Sci.* **1996**, *6*, 15–50.

(43) Kresse, G.; Furthmüller, J. Efficient iterative schemes for ab initio total-energy calculations using a plane-wave basis set. *Phys. Rev. B* **1996**, *54*, 169.

(44) Kresse, G.; Joubert, D. From ultrasoft pseudopotentials to the projector augmented-wave method. *Phys. Rev. B* **1999**, *59*, 1758–1775.

(45) Fabris, S.; Vicario, G.; Balducci, G.; De Gironcoli, S.; Baroni, S. Electronic and atomistic structures of clean and reduced ceria surfaces. *J. Phys. Chem. B* **2005**, *109*, 22860–22867.

(46) Fabris, S.; de Gironcoli, S.; Baroni, S.; Vicario, G.; Balducci, G. Taming multiple valency with density functionals: A case study of defective ceria. *Phys. Rev. B* **2005**, *71*, 041102.

(47) Seriani, N.; Jin, Z.; Pompe, W.; Ciacchi, L. C. Density functional theory study of platinum oxides: From infinite crystals to nanoscopic particles. *Phys. Rev. B* **2007**, *76*, 155421.

(48) Nomiyama, R. K.; Piotrowski, M. J.; Da Silva, J. L. F. Bulk structures of PtO and PtO_2 from density functional calculations. *Physical Review B* **2011**, *84*, 100101.

(49) Schäfer, T.; Daelman, N.; López, N. Cerium Oxides without U: The Role of Many-Electron Correlation. *J. Phys. Chem. Lett.* **2021**, *12*, 6277–6283.

(50) Henkelman, G.; Uberuaga, B. P.; Jónsson, H. A climbing image nudged elastic band method for finding saddle points and minimum energy paths. *J. Chem. Phys.* **2000**, *113*, 9901–9904.

(51) Deskins, N. A.; Dupuis, M. Electron transport via polaron hopping in bulk TiO2 : A density functional theory characterization. *Phys. Rev. B* **2007**, *75*, 195212.

(52) Plata, J. J.; Márquez, A. M.; Sanz, J. F. Electron mobility via polaron hopping in bulk ceria: A first-principles study. *J. Phys. Chem. C* **2013**, *117*, 14502–14509.

(53) Castleton, C. W. M.; Lee, A.; Kullgren, J. Benchmarking Density Functional Theory Functionals for Polarons in Oxides: Properties of CeO_2. *J. Phys. Chem. C* **2019**, *123*, 5164–5175.

(54) Pastor, E.; Park, J.-S.; Steier, L.; Kim, S.; Grätzel, M.; Durrant, J. R.; Walsh, A.; Bakulin, A. A. In situ observation of picosecond polaron self-localisation in α-Fe_2O_3 photoelectrochemical cells. *Nat. Commun.* **2019**, *10*, 3962.

(55) Vaspwiki, Monopole Dipole and Quadrupole corrections. 2019; `https://www.vasp.at/wiki/index.php/Monopole_Dipole_and_Quadrupole_corrections`.

(56) Zhang, D.; Han, Z.-K.; Murgida, G. E.; Ganduglia-Pirovano, M. V.; Gao, Y. Oxygen-Vacancy Dynamics and Entanglement with Polaron Hopping at the Reduced CeO_2 (111) Surface. *Phys. Rev. Lett.* **2019**, *122*, 096101.

(57) Larsen, A. H.; Mortensen, J. J.; Blomqvist, J.; Castelli, I. E.; Christensen, R.; Dulak, M.; Friis, J.; Groves, M. N.; Hammer, B.; Hargus, C.; Hermes, E. D.; Jennings, P. C.; Jensen, P. B.; Kermode, J.; Kitchin, J. R.; Kolsbjerg, E. L.; Kubal, J.; Kaasbjerg, K.; Lysgaard, S.; Maronsson, J. B.; Maxson, T.; Olsen, T.; Pastewka, L.; Peterson, A.; Rostgaard, C.; Schiøtz, J.; Schütt, O.; Strange, M.; Thygesen, K. S.; Vegge, T.; Vilhelmsen, L.; Walter, M.; Zeng, Z.; Jacobsen, K. W. The Atomic Simulation Environment—a Python Library for Working with Atoms. *J. Phys. Condens. Mat.* **2017**, *29*, 273002.

(58) Bahn, S. R.; Jacobsen, K. W. An Object-Oriented Scripting Interface to a Legacy Electronic Structure Code. *Comput. Sci. Eng.* **2002**, *4*, 56–66.

(59) Dooling, D. J.; Broadbelt, L. J. Generic Monte Carlo Tool for Kinetic Modeling. *Ind. Eng. Chem. Res.* **2001**, *40*, 522–529.

(60) Virtanen, P.; Gommers, R.; Oliphant, T. E.; Haberland, M.; Reddy, T.; Cournapeau, D.; Burovski, E.; Peterson, P.; Weckesser, W.; Bright, J.; van der Walt, S. J.; Brett, M.; Wilson, J.; Millman, K. J.; Mayorov, N.; Nelson, A. R. J.; Jones, E.; Kern, R.; Larson, E.; Carey, C. J.; Polat, İ.; Feng, Y.; Moore, E. W.; VanderPlas, J.; Laxalde, D.; Perktold, J.; Cimrman, R.; Henriksen, I.; Quintero, E. A.; Harris, C. R.; Archibald, A. M.; Ribeiro, A. H.; Pedregosa, F.; van Mulbregt, P.; SciPy 1.0 Contributors, SciPy 1.0: Fundamental Algorithms for Scientific Computing in Python. *Nat. Methods* **2020**, *17*, 261–272.

(61) Shaikhutdinov, S.; Wan, W.; Geiger, J.; Berdunov, N.; Lopez Luna, M.; Chee, S. W.; Daelman, N.; López, N.; Cuenya, B. R. Highly Stable and Reactive Platinum Single

Atoms on Oxygen Plasma-Functionalized CeO_2 Surfaces: Nanostructuring and Peroxo Effects. *Angew. Chem. Int. Ed.* **2022**, *in press*.

(62) Jerratsch, J.-F.; Shao, X.; Nilius, N.; Freund, H.-J.; Popa, C.; Ganduglia-Pirovano, M. V.; Burow, A. M.; Sauer, J. Electron Localization in Defective Ceria Films: A Study with Scanning-Tunneling Microscopy and Density-Functional Theory. *Phys. Rev. Lett.* **2011**, *106*, 246801.

(63) Álvarez-Moreno, M.; de Graaf, C.; López, N.; Maseras, F.; Poblet, J. M.; Bo, C. Managing the Computational Chemistry Big Data Problem: The ioChem-BD Platform. *J. Chem. Inf. Model.* **2015**, *55*, 95–103.